remote sensing

Article

ER-MACG: An Extreme Precipitation Forecasting Model Integrating Self-Attention Based on FY4A Satellite Data

Mingyue Lu [1,*], Jingke Zhang [1], Manzhu Yu [2], Hui Liu [3], Caifen He [4], Tongtong Dong [1] and Yongwei Mao [1]

[1] Geographic Science College, Nanjing University of Information Science & Technology, Nanjing 210044, China
[2] Department of Geography, Pennsylvania State University, State College, PA 16802, USA
[3] School of Remote Sensing & Geomatics Engineering, Nanjing University of Information Science & Technology, Nanjing 210044, China
[4] Zhenhai District Meteorological Bureau, Ningbo 315200, China
* Correspondence: lumingyue@nuist.edu.cn

Abstract: Extreme precipitation events often present significant risks to human life and property, making their accurate prediction an essential focus of current research. Recent studies have primarily concentrated on exploring the formation mechanisms of extreme precipitation. Existing prediction methods do not adequately account for the combined terrain and atmospheric effects, resulting in shortcomings in extreme precipitation forecasting accuracy. Additionally, the satellite data resolution used in prior studies fails to precisely capture nuanced details of abrupt changes in extreme precipitation. To address these shortcomings, this study introduces an innovative approach for accurately predicting extreme precipitation: the multimodal attention ConvLSTM-GAN for extreme rainfall nowcasting (ER-MACG). This model employs high-resolution Fengyun-4A(FY4A) satellite precipitation products, as well as terrain and atmospheric datasets as inputs. The ER-MACG model enhances the ConvLSTM-GAN framework by optimizing the generator structure with an attention module to improve the focus on critical areas and time steps. This model can alleviate the problem of information loss in the spatial–temporal convolutional long short-term memory network (ConvLSTM) and, compared with the standard ConvLSTM-GAN model, can better handle the detailed changes in time and space in extreme precipitation events to achieve more refined predictions. The main findings include the following: (a) The ER-MACG model demonstrated significantly greater predictive accuracy and overall performance than other existing approaches. (b) The exclusive consideration of DEM and LPW data did not significantly enhance the ability to predict extreme precipitation events in Zhejiang Province. (c) The ER-MACG model significantly improved in identifying and predicting extreme precipitation events of different intensity levels.

Keywords: extreme rainfall nowcasting; ER-MACG; FY4A; Zhejiang

check for updates

Citation: Lu, M.; Zhang, J.; Yu, M.; Liu, H.; He, C.; Dong, T.; Mao, Y. ER-MACG: An Extreme Precipitation Forecasting Model Integrating Self-Attention Based on FY4A Satellite Data. *Remote Sens.* **2024**, *16*, 3911. https://doi.org/10.3390/rs16203911

Academic Editor: Monica Rivas Casado

Received: 2 September 2024
Revised: 16 October 2024
Accepted: 18 October 2024
Published: 21 October 2024

1. Introduction

Frequent extreme precipitation can lead to urban flooding, landslides, and other disasters, which can adversely impact society. With global warming leading to increasing frequencies and intensities of extreme precipitation events, extreme precipitation events have emerged as a critical area of research in climate change studies [1]. According to data from the World Meteorological Organization (1970–2019), there have been more than 11,000 reported disasters globally, with over two million deaths and USD 4.3 trillion in losses [2]. Among the losses, extreme precipitation events have been responsible for more than 34% of all recorded disasters, 22% of related deaths, and 57% of related economic losses [3]. Therefore, accurately forecasting extreme precipitation events is of critical importance.

Studies on extreme precipitation currently focus on understanding the physical relationship between atmospheric conditions and the formation of extreme precipitation.

Traditional methods of predicting extreme precipitation primarily consist of dynamical and statistical models. Dynamical models establish quantitatively defined mathematical models of dynamics to study the evolution patterns of systems. They are typically used to assess the intensity, frequency, and spatial distribution of extreme precipitation events to predict the occurrence of extreme precipitation. Bremnes et al. (2004) proposed a precipitation percentile forecasting approach based on numerical weather prediction (NWP) models [4]. NWP models have difficulty capturing the spatial relationships in complex extreme precipitation phenomena and show significant uncertainties in estimating precipitation [1,5], since these systems estimate atmospheric conditions within localized areas over defined time intervals [6]. To address such limitations, Asadieh et al. (2014) studied the impact of different resolutions and physics parameter combinations of the Weather Research and Forecasting (WRF) model, optimizing configurations of the WRF model over the Loess Plateau [7]. In addition, significant developments in weather forecasting incorporated mutual influences between various elements of the global climate system, utilizing global dynamic models coupled with air-sea-land interaction mechanisms to conduct long-term trend and extreme event projection studies on climate change. For example, Ou et al. evaluated the ability of global climate models to simulate extreme precipitation in China, with the results indicating that regional climate characteristics determine the variability in simulations [8].

Statistical models offer alternative methodologies for predicting extreme precipitation. Bodri and Čermák (2000) employed an artificial neural network (ANN) method to analyze long-term historical precipitation data [9]. Wang and Ding proposed a new framework that incorporates hierarchical learning of climate system spatiotemporal patterns via clustering and classification methods [10]. Di et al. classified precipitation data using clustering and K-nearest neighbors (KNNs) methods to establish predictive models [11]. Lovino et al. employed multiple approaches, including the standardized precipitation index (SPI), principal component analysis (PCA), and singular spectrum analysis (SSA), to analyze the changing patterns of extreme precipitation in northeastern Argentina from 1901 to 2010 [12]. Additionally, Wehner et al. applied statistical extreme value theory methods to evaluate the characteristics and changes in extreme precipitation between different periods, as simulated by climate models [13]. Despite extensive application of these existing methods over the past 20 years, they frequently perform poorly in addressing stochastic and nonlinear characteristics. They are often constrained by several factors, including low spatiotemporal resolution in forecasts, significant model uncertainty, and difficulty in precisely quantifying the accuracy of predicted precipitation amounts.

The rapid advancement in artificial intelligence and big data in the 21st century have greatly impacted various industries, including meteorology. Traditional forecasting methods are increasingly inadequate for managing the vast amount of data produced daily by satellites and ground stations. In response, deep learning technologies, known for their robust nonlinear pattern recognition capabilities, are being leveraged to enhance data processing and value extraction. Deep convolutional neural networks (DCNNs) have been used to predict spatiotemporal extreme events in nonlinear physical systems [14], and long short-term memory (LSTM) networks have been proven to be more accurate at predicting extreme events, even if those events were not included during the training period [15]. Shi et al. (2015) proposed a convolutional long short-term memory network (ConvLSTM) to address the critical challenge of spatiotemporal sequence prediction in precipitation forecasting [16]. Using ConvLSTM as the encoder and multiscale convolutional layers as the decoder can effectively extract temporal information and spatial details from meteorological radar echo data [17]. Bi et al. (2023) proposed a model combining vector-quantized generative adversarial networks and transformers (VQGAN+Transformer) with an extreme value loss function [18]. In recent years, generative adversarial network (GAN) models have achieved remarkable results in predicting extreme precipitation events [19,20], due to their dual-network architecture for accurately simulating the detailed spatial and temporal variations in weather patterns and their ability to improve continuously through the adversarial training process for predicting complex phenomena. For example, Rojas-Campos et al. developed a conditional generative adversarial network (CGAN) to directly map low-resolution precipitation data from NWP model outputs [21]. However, while widely applied for indirect forecasting of extreme precipitation, existing prediction models cannot directly capture and predict short-term extreme precipitation events, and focus on hourly and daily timescales, limiting their ability to identify the detailed variations in short-term extreme precipitation events.

Advances in remote sensing technology have significantly enhanced spatial coverage and continuous measurement capabilities, making it possible for global high-resolution precipitation observations. Despite the potential, most existing studies utilize data with a temporal resolution of 30 min or lower, which fails to capture the details of rapid changes in rainfall intensity seen in the life cycle of convective heavy precipitation cells, typically less than 30 min [22]. As a result, prolonged precipitation events lasting two days may result in the reporting of two distinct intensity maps [23]. The FY4A QPE product possesses exceptionally high temporal and spatial vertical resolutions of 5 min and 4 km, enabling it to accurately capture rapid changes in precipitation over short time intervals and detailed spatial distributions. Compared to other satellite precipitation datasets, FY4A QPE demonstrates significant advantages in both timeliness and precision. For instance, the Global Precipitation Measurement (GPM) data have temporal and spatial vertical resolutions of 30 min and 10 km, respectively, while the Tropical Rainfall Measuring Mission (TRMM) offers temporal and spatial vertical resolutions of 3 h and 25 km, which limits their effectiveness in monitoring localized heavy precipitation events. Moreover, the FY4A QPE product exhibits a high correlation with station observational data for heavy precipitation events [24]. Despite the widespread use of FY4A QPE data in precipitation analysis research, their primary application has been focused on quality assessment with other satellite products [25,26], with limited application in forecasting extreme precipitation events. Therefore, this study aims to develop a novel extreme precipitation forecasting model based on FY4A QPE data to address this research gap.

This paper proposes a novel ER-MACG model that integrates the local connectivity advantages of convolutional neural networks and the global perception of self-attention mechanisms. The effects of terrain factors and atmospheric physical variables on extreme precipitation were used as input to the ER-MACG model. Our contributions to extreme precipitation event forecasting are as follows:

We propose an ER-MACG model framework tailored explicitly for spatiotemporal modeling, suitable for analyzing the complex dynamics of extreme precipitation.

(1) By integrating an attention-based ConvLSTM with a GAN, we aim to address the issues of the dissipation of sequential features in ConvLSTM, exploiting sequential and spatial features.
(2) We incorporate multisource datasets to examine the mechanisms of extreme precipitation from a new perspective.
(3) By leveraging high-resolution precipitation products from China's FY4A meteorological satellite, we explore the potential application of these satellite data in precipitation forecasting, thus laying the groundwork for future research.

2. Materials

2.1. Study Area

The study area covers Zhejiang Province and its surrounding regions, with longitudinal and latitudinal ranges of 118°–123.2°E and 27°–31.2°N, as shown in Figure 1. Zhejiang is located in the East Asian monsoon region and has a typical oceanic monsoon climate. The terrain rises from northeast to southwest. The climate is characterized by concentrated plum rain and an uneven distribution of precipitation. In addition, rainstorms and heavy rainfall are prone to occur in summer, and extreme precipitation events occur frequently in some areas. Therefore, accurate prediction of extreme precipitation is crucial for meteorological warning and disaster reduction in this region.

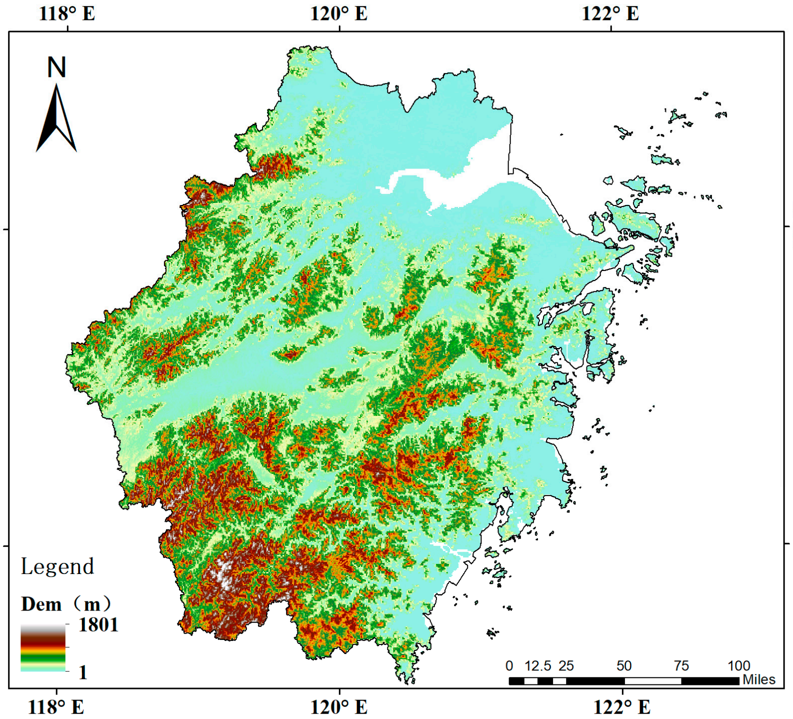

Figure 1. The location and terrain of Zhejiang, China.

2.2. Data

The FY4 series of satellites was launched at the end of 2016, representing China's second-generation geostationary meteorological satellite and replacing the FY2 series. FY4A was the first scientific experimental satellite of the FY4 series, which has relatively high temporal and spatial vertical resolutions of 5 min and 4 km, respectively, that aim to improve the effectiveness of monitoring, providing warnings for, and predicting high-impact weather events. With the continuous expansion of the influence of FY series satellites and their great potential in adverse weather monitoring, it has become increasingly necessary to study the precipitation products of FY series satellites [27]. In this study, the dataset was constructed using three different data types. These products included QPE products and layered precipitable water (LPW) products for regional China estimated in real time by the advanced geosynchronous radiation imager (AGRI) infrared channel of the FY4A satellite, as well as digital elevation model (DEM) data. Previous studies have shown that each of these three types of data is critically important for predicting extreme precipitation events [28,29]. In this study, QPE data offered estimates of rainfall intensity during extreme events; LPW data provided the humidity field characteristics of the atmosphere before and during heavy rains; and DEM data provided terrain information indispensable for the analysis.

2.2.1. Data Sources

The FY4A QPE product is a quantitative weather forecasting and climate prediction product derived from the FY4A satellite. The China Meteorological Administration (http://satellite.nsmc.org.cn (accessed on 31 October 2023)) provides real-time FY4A QPE data with a temporal resolution of 15 min or even a few minutes and a spatial resolution of 0.04° × 0.04°. This study adopted the QPE product provided by the FY4A satellite across China from May to October each year from 2019 to 2023 [30,31]. This product has a high temporal resolution of 5 min and a high spatial resolution of 4 kilometers.

The LPW product data, derived from FY4A satellite observations, represent the vertical distribution of water vapor content across atmospheric columns. This dataset provides a comprehensive understanding of the water vapor dynamics critical to the formation and evolution of extreme precipitation events. To ensure the spatial–temporal matching of the QPE and LPW product data, we selected the lower atmospheric water vapor content data provided by the LPW product from May to October 2019–2023 for analysis. The data were consistent with the QPE data in the previous section and were downloaded from the National Meteorological Information Center website.

The DEM was obtained from the global dataset provided by the National Aeronautics and Space Administration (https://www.nasa.gov/ (accessed on 31 October 2023)). The DEM serves as a digital representation of terrain elevation, generated through digitization and processing of terrain elevation data, illustrating the undulations of the terrain in a specific region through elevation values. Previous studies have shown that terrain exerts a notable impact on the spatial distribution of precipitation in complex terrain areas [32].

2.2.2. Dataset Overview

In relevant studies, the common standard definition for extreme precipitation events is events where the accumulated precipitation exceeds a predetermined threshold [33]. This study experimentally adopted the commonly used "99th percentile" method in relevant research to define extreme precipitation events as those where the accumulated precipitation exceeds the 99th percentile. The related experiments are detailed in Section 4.3. Based on the distribution of precipitation across all samples, the 99th percentile value of precipitation is calculated, as illustrated in Figure 2. A precipitation event is defined as starting from the first sample with precipitation and continuing until the next sample without precipitation. If the maximum 5-min precipitation within a precipitation event exceeds this 99th percentile value, the entire precipitation event is classified as an extreme precipitation event in this study. Furthermore, to distinguish between different events, this study defines the shortest interevent period between two extreme precipitation events as 2 h. If the interval between two precipitation events exceeds the shortest interevent period, then the two precipitation events are considered to be independent, as shown in Figure 3. Finally, based on the aforementioned method, the extreme precipitation threshold adopted in this study was calculated as an accumulated precipitation of 18 mm within a 5-min period.

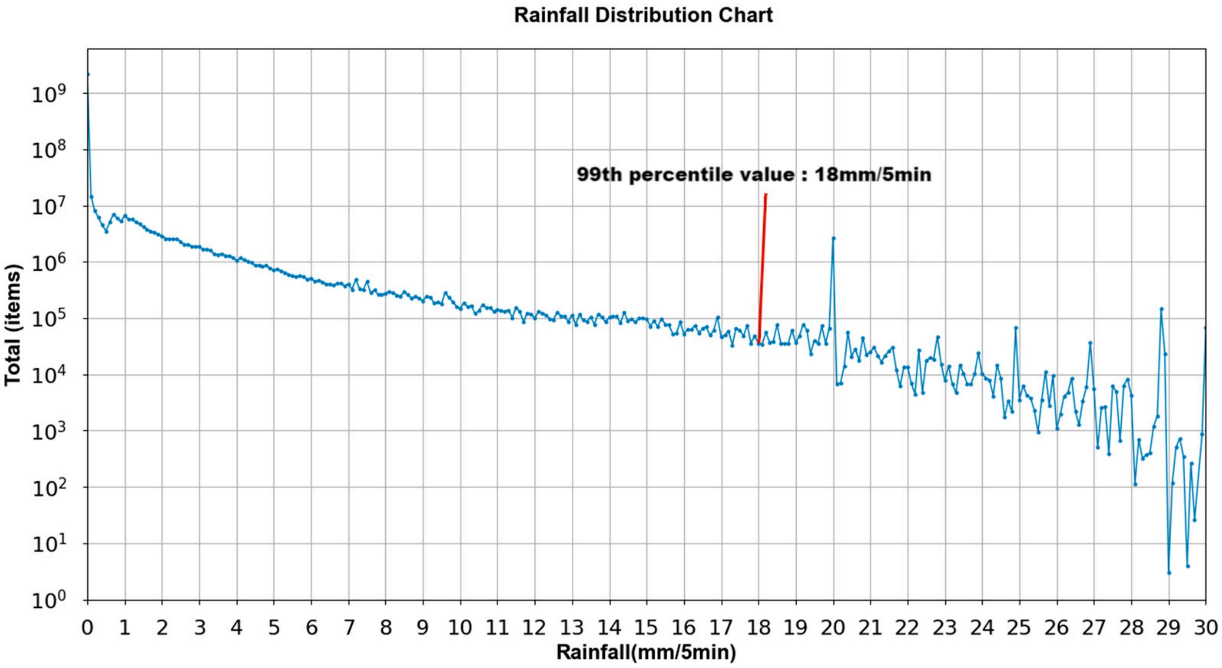

Figure 2. Distribution of precipitation values.

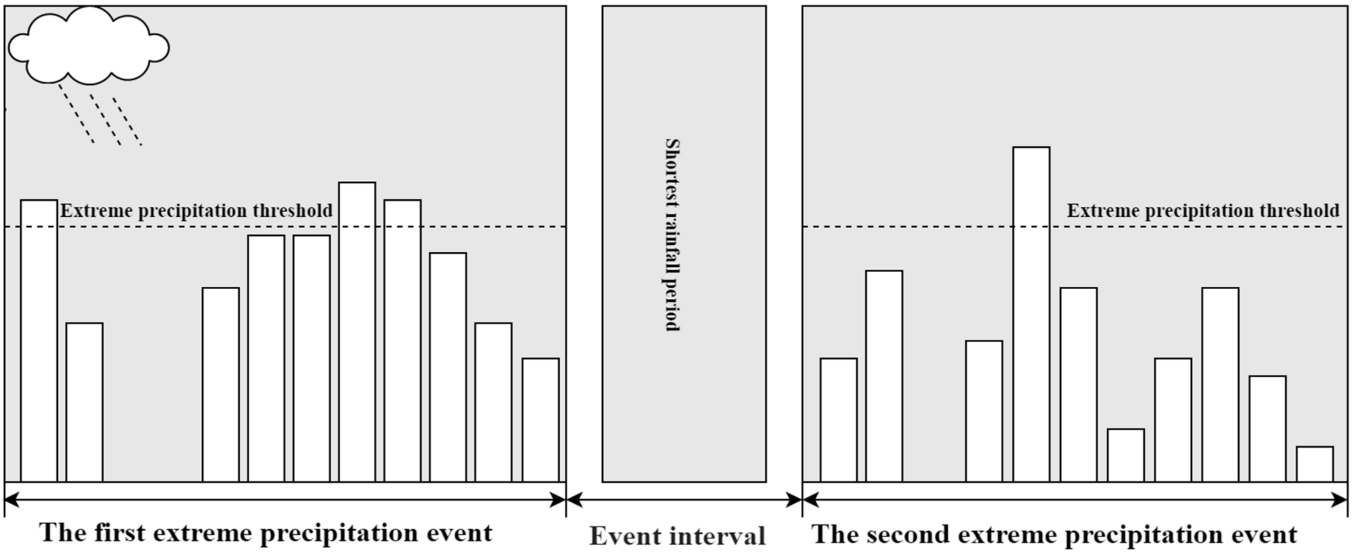

Figure 3. Identification of independent extreme precipitation events.

To fulfill the requirements of our subsequent precipitation forecasting model for continuous time series data, this study removed outliers in the QPE and LPW data obtained from the Fengyun-4A satellite. The dataset was created as follows: First, considering the large volume of raw data, the QPE images were subjected to data noise filtering in the study, and observation points with precipitation values accounting for less than 1% of the image were removed. Subsequently, based on the sequential records of the original QPE data, after removing observation points with precipitation values below 1%, all continuous precipitation sequences were extracted and individually saved in separate folders. Then, according to the definition of extreme precipitation events in the paper, all extracted precipitation sequences were screened, and those with a maximum precipitation exceeding the extreme precipitation threshold within 5 min were identified as extreme precipitation events. Additionally, to account for changes in air humidity before and after extreme precipitation events, the study added half-hour precipitation observation images before and after each extreme precipitation event, totaling six images. Finally, using the QPE time series as a reference, this study employed a sliding window approach with a time step of one to construct 20 consecutive sequences for each extreme precipitation event, consisting of 10 input images and 10 predicted precipitation observation images. To ensure consistency in the spatiotemporal dimensions of the three preprocessed datasets, QPE, LPW, and DEM, synchronized preprocessing was conducted. This preprocessing step involved uniform resampling of the time axis, normalization of each indicator value to eliminate discrepancies, and vertical stacking in chronological order to generate multidimensional spatiotemporal datasets. Through the aforementioned operations, comparability between different physical quantities was achieved, resulting in coherent and complete precipitation time series. The obtained samples were divided into training, validation, and testing sets at a ratio of 7:2:1.

3. Methods and Experiments

3.1. Methods

This study proposes using the ER-MACG model constructed on the GAN framework using a ConvLSTM network with an integrated self-attention module as the generator. This setup enables the model to recognize the temporal dependencies in precipitation sequences and enhances its focus on critical spatial areas and time steps through the attention module. The model can automatically extract and integrate rich spatiotemporal pattern information from historical multisource observation data to generate highly accurate extreme precipitation forecast results.

3.1.1. Attention-Integrated ConvLSTM

ConvLSTM is a variant of LSTM [16] that replaces the linear operations in standard LSTM with convolutional operations, capturing long-term dependencies from both temporal and spatial perspectives. This study builds upon the work proposed by Liu et al. [34] and further proposes Attention-Integrated Convolutional LSTM (Att-ConvLSTM) as a component of the model. This inclusion allows the model to concurrently learn the temporal dependencies in precipitation sequences while utilizing Att-ConvLSTM to enhance the network focus on important spatial locations and time steps. The Att-ConvLSTM model is shown in Equation (1).

$$\begin{aligned}
&\overline{X}_t = Att(X_t), \overline{H}_{t-1} = Att(H_{t-1}) \\
&i_t = \sigma(W_{xi} \times \overline{X}_t + W_{hi} \times \overline{H}_{t-1} + b_i) \\
&f_t = \sigma(W_{xf} \times \overline{X}_f + W_{hf} \times \overline{H}_{t-1} + b_f) \\
&g_t = \tanh(W_{xc} \times \overline{X}_t + W_{hc} \times \overline{H}_{t-1} + b_c) \\
&c_t = f_t \circ c_{t-1} + i_t \circ g_t \\
&o_t = \sigma(W_{xo} \times \overline{X}_t + W_{ho} \times \overline{H}_{t-1} + b_o) \\
&H_t = o_t \circ \tanh(c_t)
\end{aligned} \tag{1}$$

where Att refers to the attention module and $\overline{X}$ and $\overline{H}$ are features aggregated by the self-attention module. The attention module processes the features at each position of the input feature map at each time step. The attention module first applies linear projections to individually map the features at each position into Query (Q), Key (K), and Value (V) spaces. It then computes the similarity between the query and all keys, yielding an attention weight matrix. The given matrix reflects the degrees of dependency among different positions. Subsequently, by leveraging the attention weight matrix, the module conducts a weighted summation of the values at different positions, thereby aggregating the global contextual information of the input features and deriving a new feature representation to capture global dependency relationships. The structure of Att-ConvLSTM is shown in Figure 4.

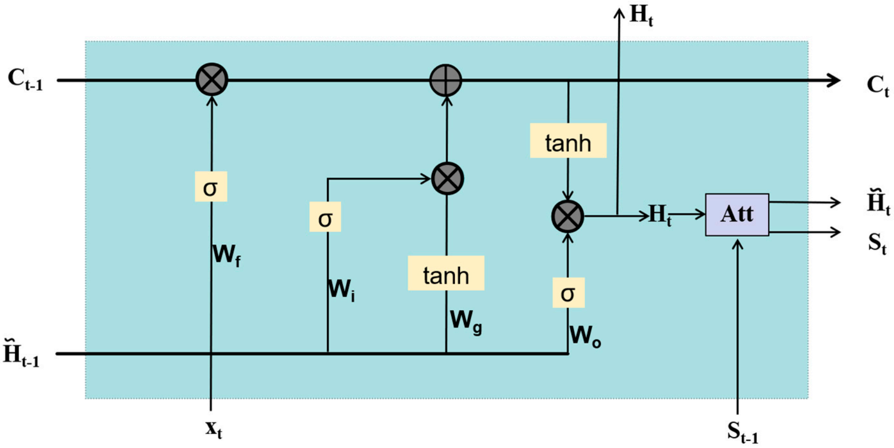

Figure 4. The structure of Att-ConvLSTM.

This paper proposes an attention module, Att, that accounts for features at each time step while also processing the full input sequence rather than a single time step. The structure of the Att module is shown in Figure 5. Differential computation is further incorporated based on temporal attention. The attention module embeds the input features at each time step and captures the global interdependencies between time steps through a query–key attention mechanism. Additionally, it calculates the difference between the current time step features and previous time step features to obtain information regarding the degree of feature changes in the temporal dimension by computing differentials. Through the above improvements, the Att module leverages the query-key attention mechanism to extract interdependencies between each time step across the full input sequence. Simultaneously, the Att module can learn information regarding subtle degrees of feature changes in the temporal dimension. In the Att module, H_t denotes the hidden state of the ConvLSTM network at time step t, S_{t-1} represents the memory state information at the previous time step t, conv represents a 1 × 1 convolution, and Value (V), Key (K), and Query (Q) denote the three vectors. W_h denotes the weighted hidden state information obtained by using H as input and calculating through V_h, K_h, and Q_h; W_s denotes the weighted memory state information obtained by using S as input and calculating through V_s, K_s, and Q_h; and W_h and W_s are convoluted to obtain the fused feature information W. Then, W is used with the original Ht to update the gate control information, finally outputting the memory state S_t and the updated hidden $\overline{H}_t$ state at the current time step t. This study builds upon previous work by incorporating differential calculations to enhance sensitivity to local precipitation variations and improve the capability to capture extreme precipitation events.

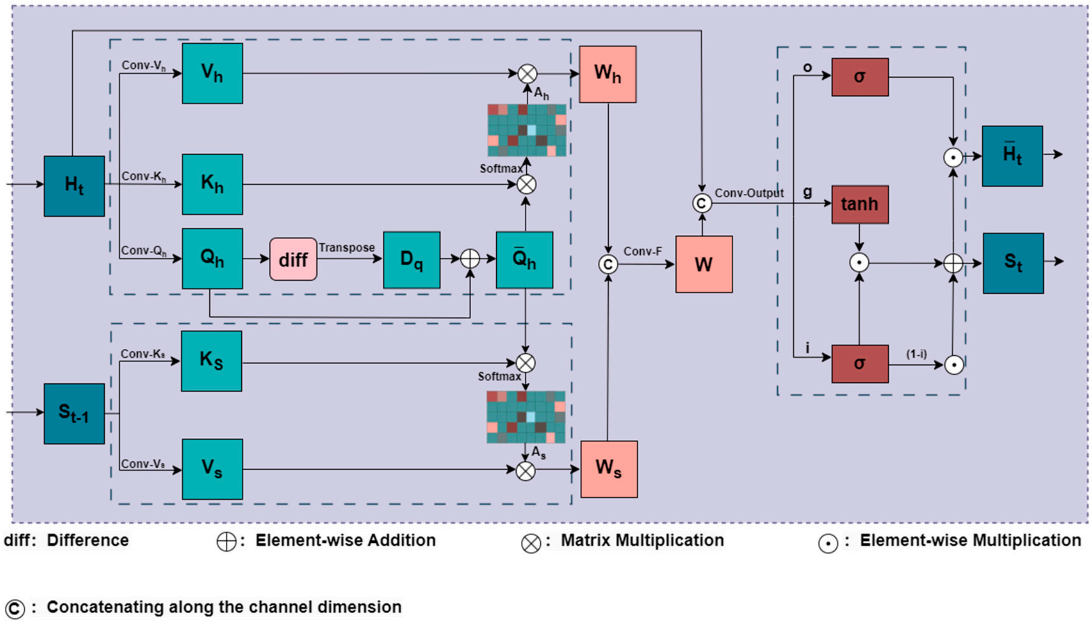

Figure 5. The structure of the Att module.

3.1.2. ER-MACG

The GAN [35] consists of a generator G and a discriminator D, which learn from each other through adversarial training. The generator G tries to generate real samples, while the discriminator D tries to distinguish between real and fake data. Through iterative training, the generator can learn the characteristics of the real data distribution and generate highly realistic real samples. The objective function of the GAN model uses the cross-entropy loss function shown in Equation (2):

$$V(D,G) = \frac{1}{\mathrm{m}}\sum_{\mathrm{i}=1}^{\mathrm{m}}[\log D(x_i) + \log(1 - D(G(z_i)))] \tag{2}$$

where x_i denotes any real data, Z_i signifies any random data with the same structure as the real data, $G(Zi)$ represents the fake data generated based on Z_i in the generator, $D(x_i)$ represents the result judged by the discriminator on the real data $\mathrm{x_i}$, and $D(G(z_i))$ represents the result judged by the discriminator on the fake data $G(z_i)$.

In designing the ER-MACG model proposed in this study, a four-layer convolutional neural network is employed as the encoder to extract multilevel feature representations. Specifically, the encoder network utilizes multiple consecutive convolutional blocks with uniformly set parameters for feature extraction. Each convolutional block consists of a convolutional layer and an activation layer, employing 5 × 5 convolution kernels for downsampling. Through consistently designed multistage downsampling, the encoder can gradually extract the spatial information of feature maps from the input layer in a hierarchical manner. Subsequently, a multilayer transposed convolutional network is employed as the decoder. The decoder gradually reconstructs the encoded data to the same resolution as the input data through multiple upsampling layers. The key design of the generator in this model lies in embedding equal amounts of Att-ConvLSTM networks between the encoder and decoder. The input and output cross-connections between multiple Att-ConvLSTM units enable the learning of temporal dependencies between different channels. During feature extraction and reconstruction by the encoder and decoder, the ability to discover interchannel spatial relationships is enabled by retaining multichannel representations within the computations of the encoder and decoder. Ultimately, this design achieves deep compression and extraction of features across both temporal and spatial dimensions.

The discriminator consists of a feature extraction layer and a fully connected classification layer. The feature extraction layer contains two 3D convolutional modules, which extract the temporal and spatial dependencies of the input sequence through multilayer downsampling. Specifically, the last 3D convolutional layer performs global average pooling on the feature maps to reduce the spatial dimension and then flattens the pooled features to obtain a 1D feature vector. These feature vectors are then fed into the subsequent fully connected classification layer, which uses the fully connected layer to predict feature classification. Through adversarial training, the generator and the discriminator iteratively train against each other, gradually improving each other's performance. The generator gradually generates more realistic samples to mislead the discriminator, while the discriminator's judgment capability is also enhanced. Through iterative adversarial training, the generator and the discriminator reach equilibrium, ultimately achieving the goal of generating real samples and jointly improving the performance of the adversarial generative model. The structure and data flow of ER-MACG are shown in Figure 6.

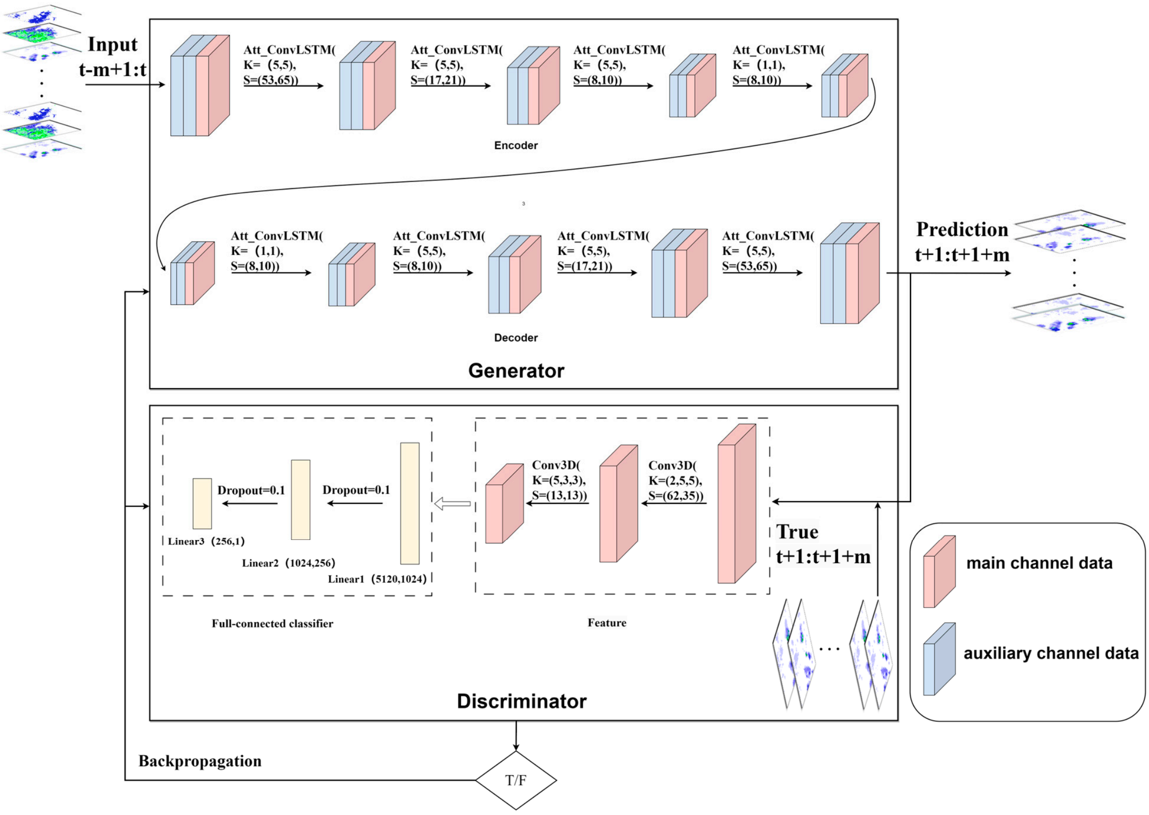

Figure 6. The structure and data flow of ER-MACG. t – m + 1, where t represents the past m frames of images at time t and t + 1:t + 1 + m represents the future m frames of images at time t.

3.2. Design of Loss Function

In real precipitation scenarios, different intensity levels of rainfall, ranging from light rain to heavy downpours or torrential rain, can co-occur in the same area and time. This study adopts a weighted approach based on the precipitation amount to address this issue. Specifically, higher weights are assigned to regions with higher precipitation amounts. This design allows the model training process to prioritize areas with greater rainfall intensity. This approach effectively tackles the challenge of accurately predicting extreme precipitation events. The loss function formula of the generator is as follows:

$$\begin{aligned} W_m &= W_1 + (W_2 - W_1) + \cdots + (W_\mathrm{m} - W_{m-1}) \\ MSE &= \Sigma_i^N \Sigma_h^H \Sigma_w^W W_{i(h,w)} \left(X_{i(h,w)} - Y_{i(h,w)}\right)^2 \\ MAE &= \Sigma_i^N \Sigma_h^H \Sigma_w^W W_{i(h,w)} \left|X_{i(h,w)} - Y_{i(h,w)}\right| \\ \mathrm{Loss} &= \alpha \times (MSE + MAE) \end{aligned} \tag{3}$$

where X represents the predicted precipitation value, Y represents the observed precipitation value from satellites, H represents the height channel, W represents the width channel, N represents the batch size, and Σ_H and Σ_W represent the sum of the height H and width W dimensions, respectively. The weights are calculated based on the cumulative difference in weights between threshold intervals in which the observed precipitation values fall, where m represents the number of threshold groups. α is a scaling factor included to prevent excessive loss values from affecting model training via gradient descent. The scaling factor in this study is set to 1×10^{-8}.

For the discriminator, this study adopts the binary cross-entropy loss function commonly used in binary classification problems. Cross-entropy is used to measure the disparity between the predicted distribution and the true distribution. The formula for the binary cross-entropy loss function is as follows:

$$L(Y, X) = -\frac{1}{N} \sum_{i=1}^{N} \left(Y_i \log(X_i) + (1 - Y_i) \log(1 - X_i)\right) \tag{4}$$

where X represents the predicted precipitation value, Y represents the observed precipitation value from satellites, and N represents the sample size.

3.3. Experiments

To comprehensively evaluate the model's performance in predicting extreme precipitation, this study utilized both statistical prediction metrics and error measurement indicators. For the statistical prediction metrics, three widely used indicators in the field of meteorological forecasting were selected: probability of detection (POD), false alarm rate (FAR), and critical success index (CSI). For the error measurement indicators, three commonly used error evaluation metrics were adopted: R, RMAE, and MAE. The following will provide detailed introductions for the aforementioned indicators.

POD: The probability of detection is used to measure the consistency between the predicted precipitation and the actual precipitation. It is the ratio of the number of correctly predicted precipitation samples to the total number of samples with actual precipitation. The higher the POD value is, the more accurate the model's prediction of real precipitation is.

$$POD = \frac{TP}{TP + FN} \tag{5}$$

where TP represents the number of samples with actual precipitation that were correctly predicted as precipitation, and FN represents the number of samples with actual precipitation that were incorrectly predicted as non-precipitation.

FAR: The false alarm rate serves to assess the rate of false alarms in precipitation prediction. It is calculated as the ratio of the number of incorrectly predicted precipitation events to the total number of precipitation predictions made by the model. It ranges from 0 to 1, with lower values indicating a greater ability of the model to avoid overpredicting precipitation.

$$FAR = \frac{FP}{FP + TP} \tag{6}$$

where FP represents the number of samples with no precipitation that were incorrectly predicted as precipitation.

CSI: The critical success index is a holistic metric that combines the POD and the FAR to assess the overall alignment between the forecasted precipitation and the observed precipitation. It ranges from 0 to 1, with higher values indicating a stronger balance achieved by the model in correctly identifying precipitation events while minimizing false alarms.

$$CSI = \frac{TP}{TP + FP + FN} \tag{7}$$

The error measurement indicators employed include the correlation coefficient (R), which can accurately reflect the linear correlation and goodness-of-fit between the predicted data and the FY4A QPE data. The root mean square error (RMSE) reflects the degree of dispersion between the predicted and observed data, providing a robust measure of the overall prediction accuracy. Additionally, the mean absolute error (MAE) captures the average magnitude of the differences between the predicted and FY4A QPE data, providing a straightforward evaluation of the model's average prediction precision. The calculation formulas for R, RMSE, and MAE are provided below.

$$\begin{aligned} R &= \frac{\sum\limits_{i=1}^{m} (\mathrm{X}_i - \overline{\mathrm{X}})(\mathrm{Y}_i - \overline{\mathrm{Y}})}{\sqrt{\sum\limits_{i=1}^{m} (\mathrm{X}_i - \overline{\mathrm{X}})^2 (\mathrm{Y}_i - \overline{\mathrm{Y}})^2}} \\ RMSE &= \sqrt{\frac{1}{m} \sum\limits_{i=1}^{m} (X_i - Y_i)^2} \\ MAE &= \frac{\sum\limits_{i=1}^{m} |X_i - Y_i|}{m} \end{aligned} \tag{8}$$

where X_i represents the predicted precipitation amount, Y_i represents the satellite-observed precipitation amount, $\overline{X}$ and $\overline{Y}$ are the respective mean values of the model predictions and satellite observations, respectively, and m is the number of precipitation observations.

A series of sensitivity analysis experiments were designed to investigate the influence of terrain data and physical factors on extreme precipitation. Different combinations of terrain data and physical variables were adjusted as input data (Table 1). To fully evaluate the advantages of the ER-MACG model in this task, a comparison was made with several commonly used deep learning models, including ConvLSTM, ConvLSTM-GAN, and Swin Transformer [36]. All the comparative models were configured with consistent settings, including using a single precipitation input channel, an initial learning rate of 0.001, 62 training iterations, and a 7:2:1 ratio for the training, validation, and test sets, respectively.

Table 1. Description of the sensitivity analysis experiment.

Input Features	FY4A QPE	DEM	LPW
ER-MACG (One)	√	×	×
ER-MACG (Two)	√	√	×
ER-MACG (Three)	√	√	√

4. Results and Discussion

4.1. Model Performance Evaluation

Table 2 displays the average scores of the evaluation metrics for the prediction outcomes of the next ten frames in extreme precipitation events for the four models. Among these metrics, the POD, FAR, CSI, R, RMSE, and MAE of the ER-MACG model are better than those of the other three models. These results indicate that despite using the same number of iterations, the ER-MACG model demonstrates better predictive accuracy because of the attention module. Currently, the ER-MACG model has not yet fully converged, indicating that additional iterations are required to complete the training process. However, even at this point, the ER-MACG model exhibits lower prediction errors across all evaluation metrics, proving its predictive accuracy. The ConvLSTM-GAN model also showed improvement over the singular ConvLSTM model, highlighting the importance of model architecture in enhancing prediction outcomes. Overall, the comprehensive superiority of the ER-MACG model across all metrics demonstrates that it has significantly better overall performance than the other three models.

Table 2. Quantitative evaluation of POD (%), FAR (%), CSI (%), R (%), RMSE, and MAE for different methods.

	Average Score for the Next Ten Frames					
Method	**POD**	**FAR**	**CSI**	**R**	**RMSE**	**MAE**
Swin Transformer	0.732	0.328	0.539	0.792	1.495	0.514
ConvLSTM	*0.842*	0.505	0.452	0.629	2.002	0.670
ConvLSTM-GAN	0.823	*0.282*	*0.621*	*0.809*	*1.445*	*0.448*
ER-MACG (One)	**0.857**	**0.278**	**0.644**	**0.835**	**1.349**	**0.408**

Note: The best and second-best metrics are indicated with bold and italics, respectively.

The results of Figure 7 indicate that when comparing the variation trends in six key predictive performance metrics of different forecasting methods over a 50-min time span, the ER-MACG model outperforms the other models at most time points, albeit with slight differences. Specifically, at the 10th, 15th, and 50th minutes, the POD of the ER-MACG model is slightly lower than that of the ConvLSTM model, and at the 35th min, its FAR is marginally greater than that of the ConvLSTM-GAN model. These minor differences highlight the performance of the model under specific conditions. Overall, the ER-MACG model demonstrates good performance across all the evaluation metrics, particularly for the other four indicators, reflecting its comprehensive advantages in prediction accuracy and error minimization.

The analysis shows that the ER-MACG model outperforms other models on most metrics, and slight variations in performance at specific time points do not affect its overall superiority. This finding further emphasizes the significant comprehensive performance advantage of this model in precipitation forecasting, especially in accurately capturing precipitation dynamics and minimizing forecast errors.

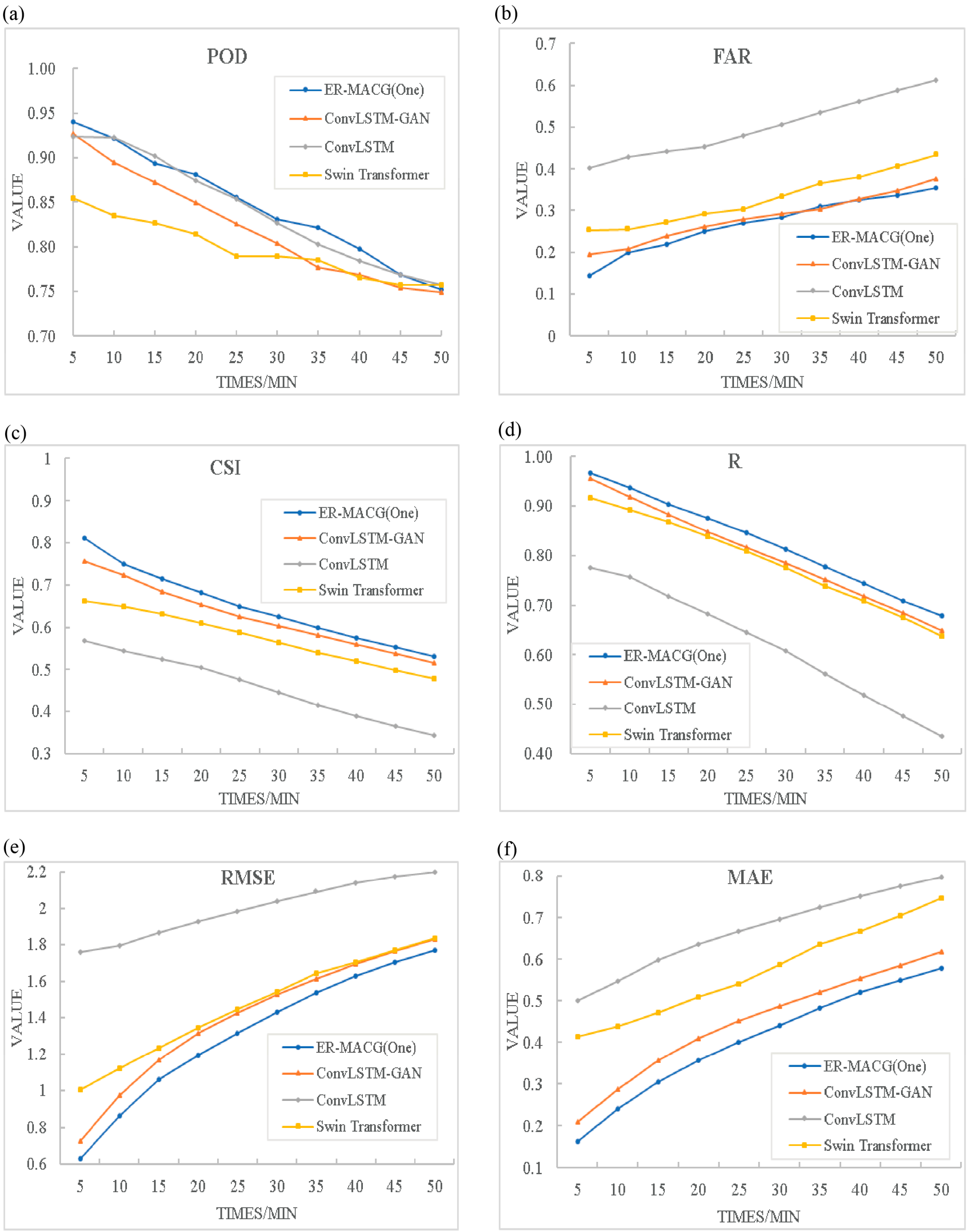

Figure 7. Evaluation curves of the POD (**a**), FAR (**b**), CSI (**c**), R (**d**), RMSE (**e**), and MAE (**f**) performance metrics for different forecasting methods over 50 min.

4.2. Sensitivity Analysis of the Input Data

In this section, the impacts of LPW and DEM data on the accuracy of extreme precipitation event forecasts in the Zhejiang region are investigated. This section also considers the advantages of introducing an attention mechanism module, namely, focusing on relevant information while ignoring irrelevant information. Although historical research has highlighted the potential value of DEMs in precipitation forecasting [37], the experimental results of this study did not indicate that the inclusion of LPW and DEM data significantly improved forecast accuracy. In particular, the inclusion of DEM data did not result in a marked enhancement of the ER-MACG (Two) model's accuracy in predicting extreme precipitation in Zhejiang, underscoring the limited efficacy of standalone DEM data in significantly improving forecast precision for extreme events in this region. Research has shown that the interaction between the central circulation of typhoons and local topography leads to heavy precipitation [38]. The interplay among mesoscale convective systems, mountainous terrain, and sea surface temperature is a key factor in the formation of precipitation in Zhejiang [39,40]. Furthermore, the analysis of the cumulative precipitation distribution (as shown in Figure 8) further confirms that extreme precipitation events tend to occur in coastal lowlands and are closely related to factors such as atmospheric circulation and sea surface temperature. Therefore, in future predictions of extreme precipitation in the Zhejiang region, greater attention should be given to the combined effects of large-scale meteorological factors related to typhoons, including atmospheric circulation and sea surface temperature.

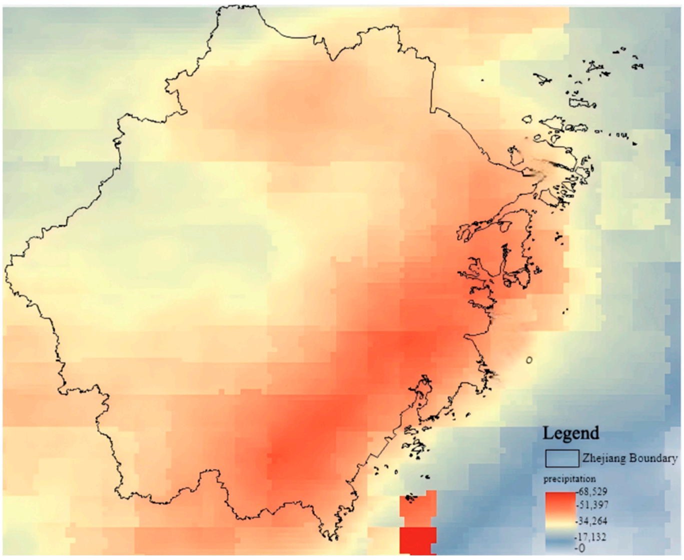

Figure 8. Cumulative precipitation distribution map for rainfall exceeding 18 mm/5 min from May to October 2018–2023.

4.3. Impact of Extreme Precipitation Event Thresholds on Forecasting

Table 3 presents the performance metrics for forecasting extreme precipitation events defined by the 95th, 97th, and 99th percentile thresholds of 5-min cumulative rainfall. Utilizing various threshold values leads to the selection of training data with different quantities and intensities of extreme precipitation events. The choice of percentile threshold significantly influences predictive outcomes due to regional characteristics. The experimental findings indicate that using the 95th percentile threshold improved only the POD metric. The R and RMSE metrics for the 97th percentile threshold were similar to those for the 99th percentile, with minimal differences. However, employing the 99th percentile threshold resulted in the optimal performance of the FAR, CSI, and MAE metrics, thus demonstrating the most significant improvement. Thus, this study concludes that the 99th percentile threshold is the most effective for defining extreme precipitation events as it achieves the best predictive results.

Table 3. Predictive performance at different definition thresholds.

	Average Score for the Next Ten Frames					
Threshold	**POD**	**FAR**	**CSI**	**R**	**RMSE**	**MAE**
95th Percentile	**0.878**	0.358	0.588	0.838	1.372	0.465
97th Percentile	0.852	0.312	0.614	**0.834**	**1.357**	0.431
99th Percentile	0.847	**0.270**	**0.645**	0.832	1.361	**0.403**

Note: The best metrics are shown in bold.

Moving from the 95th to the 99th percentile not only significantly enhances the data quality but also reduces the data volume, consequently decreasing the model training time. Moreover, while thresholds above the 99th percentile were explored, no additional improvement in predictive performance was observed. At this juncture, the diminished data volume started to adversely impact outcomes. This finding suggests that improving the data quality can enhance the prediction accuracy and efficiently reduce the model training duration. Thus, pinpointing this critical equilibrium between data quality and volume is essential.

4.4. Case Analysis

In this study, three cases with distinct precipitation characteristics, representing heavy (Case 2), moderate (Case 1), and light (Case 3) precipitation scenarios, were selected. Comparative analysis through image visualization results assessed the predictive performance of ConvLSTM, ConvLSTM_GAN, and the proposed ER-MACG method for each case. In Figure 9, the first three rows horizontally display the forecast results of the three methods at different time points, while the last row shows the actual precipitation data. From left to right, the images are arranged in chronological order, with varying color shades representing different levels of precipitation.

In Case 3, the ER-MACG model is able to accurately depict the distribution of precipitation in the early stages (5 to 15 min), especially in capturing the intensity and shape of precipitation edges with high precision. However, as the model's loss function assigns more weight to heavy precipitation, its accuracy in predicting light precipitation is not as high as that in moderate and heavy precipitation. This gap becomes particularly evident in Case 1, where the ER-MACG model demonstrates greater accuracy in determining the location of the precipitation core and predicting the spatial expansion of precipitation over time. In long-term forecasts of Case 2 (35 to 45 min), the performance of the ER-MACG model is especially notable, as it accurately simulates the location and morphology of high precipitation areas and aligns closely with observed precipitation intensity, reflecting its potential advantages in early warning of extreme weather events.

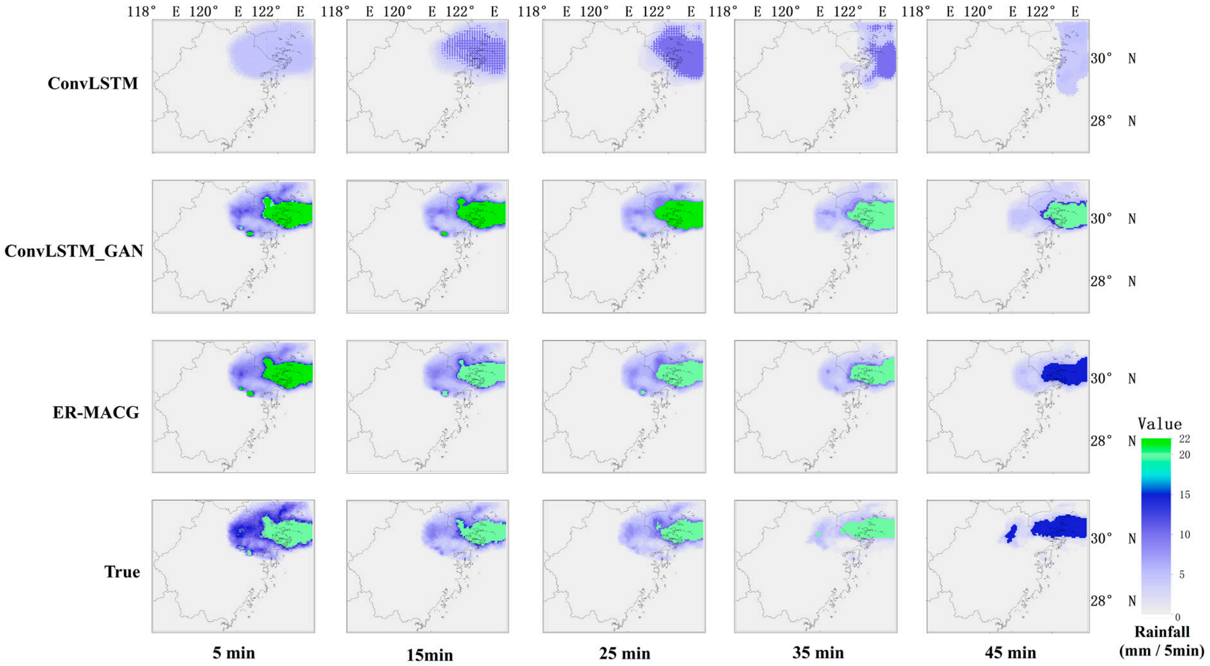

(**a**)

Figure 9. *Cont.*

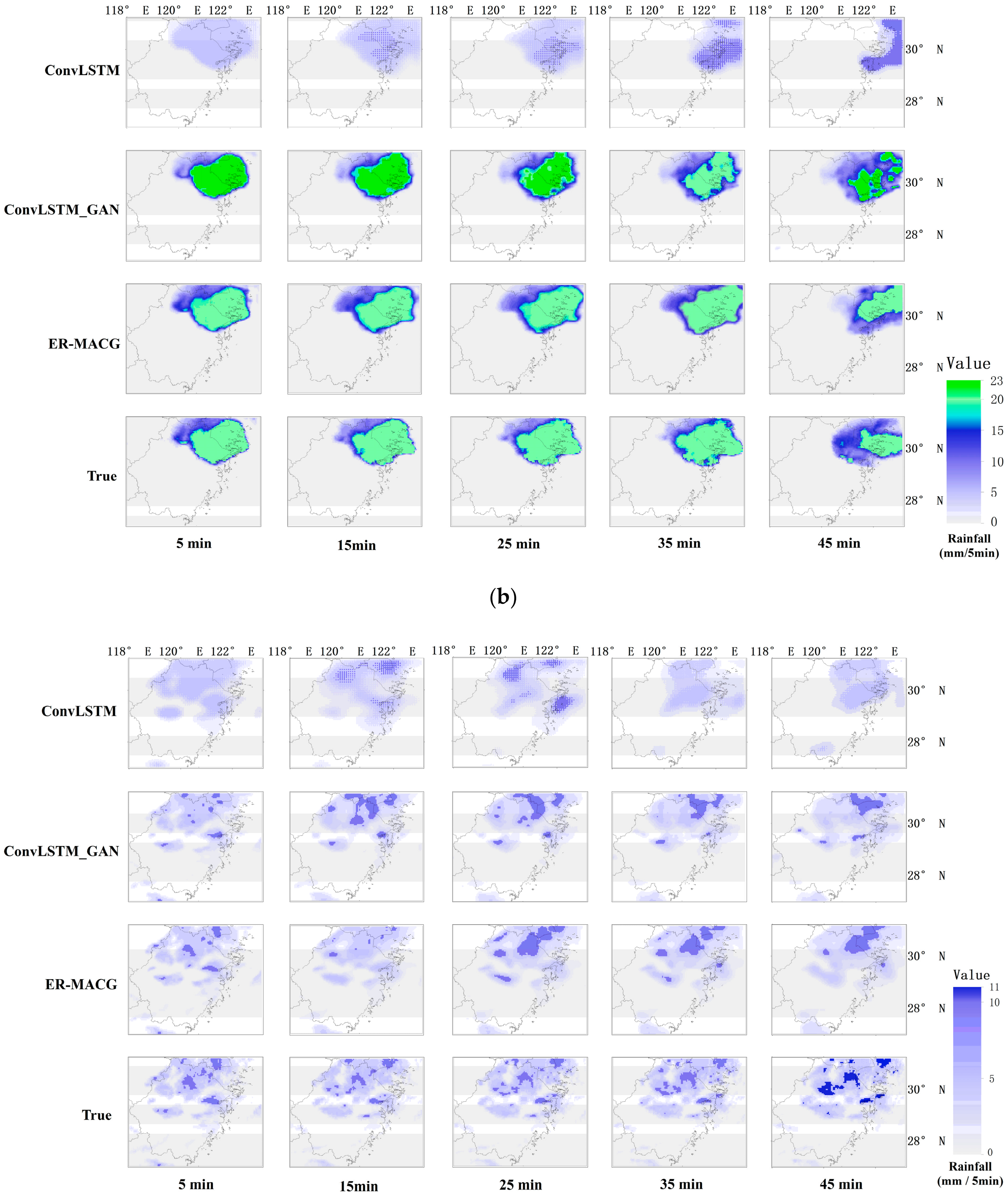

(**b**)

(**c**)

Figure 9. Comparison of Three Precipitation Intensities During Extreme Precipitation Events. (**a**) Case 1 moderate precipitation. (**b**) Case 2 heavy precipitation. (**c**) Case 3 light precipitation.

Analyzing the data in Tables 4 and 5, the performance of the ER-MACG model across the three cases is compared with that of the ConvLSTM and ConvLSTM-GAN methods. In Case 1, the ER-MACG model excels in reducing the FAR while sustaining outstanding overall performance on the CSI, R, RMSE, and MAE metrics, notably surpassing the other two methods in reducing forecast errors. In Cases 2 and 3, ER-MACG displays superior performance over ConvLSTM-GAN across nearly all metrics, particularly in reducing false alarm rates and enhancing overall prediction accuracy. In contrast, the ConvLSTM method generally exhibits higher RMSE and MAE values across all the cases, indicating larger prediction deviations. The data in Table 5 show predictions for different precipitation intensities, where the ER-MACG model maintains relatively stable performance across various precipitation levels. In contrast, ConvLSTM exhibited a rapid decline in POD values when predicting stronger precipitation events, indicating deficiencies in capturing intense precipitation events. The stability shown by ER-MACG in predicting higher levels of precipitation demonstrates robustness to different precipitation intensities.

The comprehensive analysis of forecast results for three cases of varying precipitation intensities indicates that the ER-MACG model has a lower false alarm rate and higher prediction accuracy, especially demonstrating a significant advantage in predicting moderate to heavy precipitation events. The integration of the attention mechanism provides enhanced methodological support for precipitation forecasting, particularly in handling complex precipitation events. At the same time, this model addresses the issues of precipitation dissipation seen in ConvLSTM and the over-intensification and lack of detail in heavy precipitation events characteristic of ConvLSTM_GAN.

Table 4. Quantitative evaluation of POD (%), FAR (%), CSI (%), R (%), RMSE, and MAE for different cases.

		Average Score for the Next Ten Frames					
Case 1	Method	POD	FAR	CSI	R	RMSE	MAE
	ConvLSTM	0.850	0.415	0.529	0.775	2.449	0.839
	ConvLSTM-GAN	**0.977**	*0.131*	*0.851*	*0.942*	*1.198*	*0.382*
	ER-MACG	*0.956*	**0.086**	**0.877**	**0.960**	**0.984**	**0.305**
Case 2	Method	POD	FAR	CSI	R	RMSE	MAE
	ConvLSTM	0.912	0.370	0.593	0.770	5.531	2.354
	ConvLSTM-GAN	**0.985**	*0.161*	*0.828*	*0.924*	**2.260**	*0.724*
	ER-MACG	**0.985**	**0.125**	**0.863**	**0.925**	*2.445*	**0.684**
Case 3	Method	POD	FAR	CSI	R	RMSE	MAE
	ConvLSTM	0.925	0.417	0.556	0.656	1.563	0.920
	ConvLSTM-GAN	*0.935*	*0.234*	*0.726*	*0.848*	*1.073*	**0.585**
	ER-MACG	**0.967**	**0.224**	**0.755**	**0.890**	**0.910**	*0.587*

Note: The best and second-best metrics are indicated with bold and italics, respectively.

Table 5. Quantitative evaluation of different precipitation intensities.

	Method	**Metric**	**Precipitation Intensity Level (mm/5 min)**			
			5	**10**	**15**	**18**
Case 1	ConvLSTM	POD	0.288	-	-	-
		FAR	0.161	-	-	-
		CSI	0.273	-	-	-
	ConvLSTM-GAN	POD	**0.940**	**0.933**	0.873	0.736
		FAR	0.230	0.341	0.196	0.098
		CSI	0.733	0.628	0.719	0.681
	ER-MACG	POD	0.912	0.921	**0.938**	**0.897**
		FAR	**0.203**	**0.254**	**0.190**	**0.094**
		CSI	**0.740**	**0.700**	**0.768**	**0.820**
Case 2	ConvLSTM	POD	0.254	-	-	-
		FAR	0.092	-	-	-
		CSI	0.248	-	-	-
	ConvLSTM-GAN	POD	**0.957**	**0.918**	0.793	0.656
		FAR	0.123	0.172	**0.146**	0.071
		CSI	0.844	**0.770**	0.698	0.625
	ER-MACG	POD	0.944	0.908	**0.852**	**0.810**
		FAR	**0.116**	**0.167**	0.165	**0.166**
		CSI	0.839	0.768	**0.729**	**0.698**

Note: The best metrics are shown in bold.

5. Conclusions

In this paper, the ER-MACG model, a novel short-term forecasting method for extreme precipitation that combines ConvLSTM and a GAN with an integrated attention module, is introduced. This model is designed to capture and retain all extreme precipitation events exceeding a certain threshold. By utilizing DEM and LPW data as inputs within the same spatiotemporal context, continuous predictions are obtained every 5 min for the next 50 min. The introduced weighted loss function weights different regions based on historical extreme precipitation intensities, making the model more inclined to reproduce the distribution characteristics of extreme precipitation areas when generating forecasts. By optimizing the enhanced loss function, the model can focus on areas of heavy precipitation, significantly improving the short-term forecasting performance for extreme precipitation. To evaluate the performance of the ER-MACG model for extreme precipitation forecasting, this study conducted comparative analyses with various mainstream forecasting models. Additionally, the study explored the impact of different types of input data combinations on forecasting effectiveness. The experimental results reveal the following key findings:

(1) In terms of extreme precipitation forecasting performance, the ER-MACG (One) model outperformed the comparison models in terms of the POD, FAR, CSI, R, RMSE, and MAE metrics. However, the introduction of the attention mechanism in the ER-MACG (One) model slowed the convergence speed of training, and the demand for computational resources increased accordingly. Given the relatively small scale of the study area, these potential drawbacks did not significantly impact the results of this study. However, in larger-scale forecasting areas, the ER-MACG (One) model still demonstrated potential for optimization in terms of performance and computational efficiency. This finding provides a significant reference value for future research on model optimization.

(2) Although DEM and LPW data are considered to have the potential for precipitation forecasting, this study did not observe a significant performance improvement when using them to predict extreme precipitation events in the Zhejiang region. This finding was due partly to the limitations of the spatial and temporal resolution of the FY4A QPE data, which restricted the acquisition of more extreme precipitation-related data. Due to Zhejiang Province's proximity to the ocean and its significant influence from large-scale atmospheric systems such as atmospheric circulation and typhoons, the existing DEM and LPW data are insufficient to adequately capture the dynamics and effects of these complex meteorological systems. Therefore, future forecasts of extreme precipitation in the Zhejiang region should focus on large-scale meteorological factors, such as the impact of typhoons, and explore the use of high-resolution satellite data and data fusion techniques to further optimize the accuracy of extreme precipitation forecasts in the Zhejiang region.

(3) In recent years, the academic community has increasingly favored the use of short-duration precipitation intensities exceeding a specific percentile value as the definition criterion for short-duration extreme precipitation events. However, directly adopting a fixed percentile such as 95% without empirical verification is unscientific. Considering the climatic environmental differences across regions, this study selected three representative percentiles, 95%, 97%, and 99%, in Zhejiang Province and compared the ability of each threshold to identify extreme precipitation events using actual precipitation data. The results indicate that using the 99th percentile as the threshold most accurately identifies extreme short-duration precipitation events in Zhejiang Province, providing a more scientific method for defining extreme precipitation. Therefore, it is advisable that when applying the findings of this study to other regions, one should implement adaptive modifications informed by local climatic conditions and precipitation patterns to ensure the precise identification of extreme precipitation events.

(4) When solely utilizing precipitation intensity data to drive the ER-MACG model, its performance in predicting extreme precipitation surpasses that of other comparison models. In contrast, predictions using only the ConvLSTM architecture are less effective. However, by incorporating the adversarial learning framework GAN, the model's recognition capability is significantly enhanced, highlighting the potential advantages of the GAN for this

task. Unlike the singular ConvLSTM-GAN architecture, the ER-MACG model proposed in this study integrates ConvLSTM with a GAN and an attention mechanism. The experimental results show that the ER-MACG model outperforms the singular ConvLSTM-GAN architecture across multiple evaluation metrics. Moreover, predictions under different precipitation intensities reveal that the ER-MACG model excels in predicting moderate to heavy precipitation events, further proving the effectiveness of the attention module in capturing the spatiotemporal characteristics of extreme precipitation.

With technological advancements, high-resolution spatiotemporal satellite data, especially from FY4A, have shown tremendous potential for short-term extreme precipitation forecasting, despite existing research revealing shortcomings in terms of data quality. Future studies will focus on quality assessment and in-depth inversion research of high spatiotemporal resolution satellite data such as data from FY4A to ensure data accuracy and reliability. Additionally, future research will explore atmospheric parameters closely related to extreme precipitation to enhance the interpretability and predictive accuracy of the model. Efforts will also be made to refine existing extreme precipitation forecasting models and evaluate their practical application in the Zhejiang region, aiming to provide effective technical support for extreme precipitation early warning and forecasting and to promote the further application of next-generation satellite data such as FY4A data in the field of meteorological forecasting.

Author Contributions: Conceptualizations, M.L., M.Y., H.L. and C.H.; methodology, M.L., J.Z., M.Y., and H.L.; software, J.Z. and T.D.; validation, M.L.; formal analysis, J.Z.; investigation, J.Z. and C.H.; resources, M.L. and M.Y.; data curation, J.Z.; writing—original draft preparation, M.L., J.Z. and M.Y.; writing—review and editing, M.L., M.Y.; visualization, Y.M.; supervision, M.L. and H.L.; project administration, J.Z; funding acquisition, M.L. All authors have read and agreed to the published version of the manuscript.

Funding: This paper was supported by the NSFC Project (41871285) (52104158).

Data Availability Statement: Some data, models, or code that support the findings of this study are available from the corresponding author upon reasonable request.

Conflicts of Interest: The authors declare no conflict of interest.

References

1. Tabari, H. Climate change impact on flood and extreme precipitation increases with water availability. *Sci. Rep.* **2020**, *10*, 13768. [CrossRef] [PubMed]
2. Douris, J.; Kim, G. The Atlas of Mortality and Economic Losses from Weather, Climate and Water Extremes (1970–2019). 2021. Available online: https://policycommons.net/artifacts/1850732/the-atlas-of-mortality-and-economic-losses-from-we/2597666/ (accessed on 5 April 2023).
3. Zhang, Y.; Long, M.; Chen, K.; Xing, L.; Jin, R.; Jordan, M.I.; Wang, J. Skilful nowcasting of extreme precipitation with NowcastNet. *Nature* **2023**, *619*, 526–532. [CrossRef] [PubMed]
4. Bremnes, J.B. Probabilistic forecasts of precipitation in terms of quantiles using NWP model output. *Mon. Weather Rev.* **2004**, *132*, 338–347. [CrossRef]
5. Bray, M.; Han, D.; Xuan, Y.; Bates, P.; Williams, M. Rainfall uncertainty for extreme events in NWP downscaling model. *Hydrol. Process.* **2011**, *25*, 1397–1406. [CrossRef]
6. Liguori, S.; Rico-Ramirez, M.A. Quantitative assessment of short-term rainfall forecasts from radar nowcasts and MM5 forecasts. *Hydrol. Process.* **2012**, *26*, 3842–3857. [CrossRef]
7. Asadieh, B.; Krakauer, N. Global trends in extreme precipitation: Climate models vs. observations. *Hydrol. Earth Syst. Sci. Discuss.* **2014**, *11*, 11369–11393.
8. Ou, T.; Chen, D.; Linderholm, H.W.; Jeong, J.-H. Evaluation of global climate models in simulating extreme precipitation in China. *Tellus A Dyn. Meteorol. Oceanogr.* **2013**, *65*, 19799. [CrossRef]
9. Bodri, L.; Čermák, V. Prediction of extreme precipitation using a neural network: Application to summer flood occurrence in Moravia. *Adv. Eng. Softw.* **2000**, *31*, 311–321. [CrossRef]
10. Wang, D.; Ding, W. A hierarchical pattern learning framework for forecasting extreme weather events. In Proceedings of the 2015 IEEE International Conference on Data Mining, Atlantic City, NJ, USA, 14–17 November 2015; pp. 1021–1026.
11. Di, Y.; Ding, W.; Mu, Y.; Small, D.L.; Islam, S.; Chang, N.-B. Developing machine learning tools for long-lead heavy precipitation prediction with multi-sensor data. In Proceedings of the 2015 IEEE 12th International Conference on Networking, Sensing and Control, Taipei, Taiwan, 9–11 April 2015; pp. 63–68.

12. Lovino, M.; García, N.O.; Baethgen, W. Spatiotemporal analysis of extreme precipitation events in the Northeast region of Argentina (NEA). *J. Hydrol. Reg. Stud.* **2014**, *2*, 140–158. [CrossRef]
13. Wehner, M.F. Predicted twenty-first-century changes in seasonal extreme precipitation events in the parallel climate model. *J. Clim.* **2004**, *17*, 4281–4290. [CrossRef]
14. Jiang, J.; Huang, Z.-G.; Grebogi, C.; Lai, Y.-C. Predicting extreme events from data using deep machine learning: When and where. *Phys. Rev. Res.* **2022**, *4*, 023028. [CrossRef]
15. Frame, J.M.; Kratzert, F.; Klotz, D.; Gauch, M.; Shalev, G.; Gilon, O.; Qualls, L.M.; Gupta, H.V.; Nearing, G.S. Deep learning rainfall–runoff predictions of extreme events. *Hydrol. Earth Syst. Sci.* **2022**, *26*, 3377–3392. [CrossRef]
16. Shi, X.; Chen, Z.; Wang, H.; Yeung, D.-Y.; Wong, W.-K.; Woo, W.-c. Convolutional LSTM network: A machine learning approach for precipitation nowcasting. *Adv. Neural Inf. Process. Syst.* **2015**, *28*.
17. Wu, Y.; Wei, L.; Yang, C. Decoding Feature Maps with Multi-scale Convolutional Kernels. In Proceedings of the International Conference on Computer Engineering and Networks, Haikou, China, 4–7 November 2022; pp. 1345–1353.
18. Bi, H.; Kyryliuk, M.; Wang, Z.; Meo, C.; Wang, Y.; Imhoff, R.; Uijlenhoet, R.; Dauwels, J. Nowcasting of Extreme Precipitation Using Deep Generative Models. In Proceedings of the ICASSP 2023-2023 IEEE International Conference on Acoustics, Speech and Signal Processing (ICASSP), Rhodes Island, Greece, 4–9 June 2023; pp. 1–5.
19. Ji, Y.; Gong, B.; Langguth, M.; Mozaffari, A.; Mache, K.; Schultz, M.; Zhi, X. GAN-Based Video Prediction Model for Precipitation Nowcasting. In *EGU General Assembly Conference Abstracts*; European Geosciences Union: Vienna, Austria, 2022; p. EGU22–12086.
20. Ji, Y.; Gong, B.; Langguth, M.; Mozaffari, A.; Zhi, X. CLGAN: A generative adversarial network (GAN)-based video prediction model for precipitation nowcasting. *Geosci. Model Dev.* **2023**, *16*, 2737–2752. [CrossRef]
21. Rojas-Campos, A.; Langguth, M.; Wittenbrink, M.; Pipa, G. Deep learning models for generation of precipitation maps based on numerical weather prediction. *Geosci. Model Dev.* **2023**, *16*, 1467–1480. [CrossRef]
22. Pirone, D.; Cimorelli, L.; Del Giudice, G.; Pianese, D. Short-term rainfall forecasting using cumulative precipitation fields from station data: A probabilistic machine learning approach. *J. Hydrol.* **2023**, *617*, 128949. [CrossRef]
23. Zhang, J.; Xu, J.; Dai, X.; Ruan, H.; Liu, X.; Jing, W. Multi-source precipitation data merging for heavy rainfall events based on cokriging and machine learning methods. *Remote Sens.* **2022**, *14*, 1750. [CrossRef]
24. Li, D.; Min, X.; Xu, J.; Xue, J.; Shi, Z. Assessment of three gridded satellite-based precipitation products and their performance variabilities during typhoons over Zhejiang, southeastern China. *J. Hydrol.* **2022**, *610*, 127985. [CrossRef]
25. Song, Y.; Du, T.; Zeng, B.; Wu, Q.; Wang, G. Evaluation of fengyun geosynchronous orbit and GPM satellites precipitation products over the southeastern Tibetan plateau. *Int. J. Remote Sens.* **2024**, *45*, 5616–5639. [CrossRef]
26. Yang, Y.; Ji, W.; Niu, L.; Zheng, Z.; Huang, W.; Zhang, C.; Hao, X.; Xiao, J.; Li, H. Assessing satellite and reanalysis-based precipitation products in cold and arid mountainous regions. *J. Hydrol. Reg. Stud.* **2024**, *51*, 101612. [CrossRef]
27. Xian, D.; Zhang, P.; Gao, L.; Sun, R.; Zhang, H.; Jia, X. Fengyun meteorological satellite products for earth system science applications. *Adv. Atmos. Sci.* **2021**, *38*, 1267–1284. [CrossRef]
28. Antal, A.; Dumitrescu, A.; Cheval, S.; Guerreiro, P.M. Enhanced precipitation prediction using DEM-based predictors and satellite imagery. *Int. J. Climatol.* **2023**, *43*, 2504–2520. [CrossRef]
29. Manandhar, S. GPS Signal Derived Precipitable Water Vapor and Its Applications in Rainfall Prediction. Ph.D. Thesis, Nanyang Technological University, Singapore, 2019.
30. Jin, H.; Chen, X.; Wu, P.; Song, C.; Xia, W. Evaluation of spatial-temporal distribution of precipitation in mainland China by statistic and clustering methods. *Atmos. Res.* **2021**, *262*, 105772. [CrossRef]
31. Tian, Y.; Xu, Y.-P.; Booij, M.; Lin, S.; Zhang, Q.; Lou, Z. Detection of trends in precipitation extremes in Zhejiang, east China. *Theor. Appl. Climatol.* **2012**, *107*, 201–210. [CrossRef]
32. Shu, S. Spatial estimation and impact factors of summer afternoon and evening precipitation under complex terrain. In Proceedings of the XXVIII General Assembly of the International Union of Geodesy and Geophysics (IUGG), Berlin, Germany, 1–20 July 2023.
33. McPhillips, L.E.; Chang, H.; Chester, M.V.; Depietri, Y.; Friedman, E.; Grimm, N.B.; Kominoski, J.S.; McPhearson, T.; Méndez-Lázaro, P.; Rosi, E.J. Defining extreme events: A cross-disciplinary review. *Earth's Future* **2018**, *6*, 441–455. [CrossRef]
34. Lin, Z.; Li, M.; Zheng, Z.; Cheng, Y.; Yuan, C. Self-attention convlstm for spatiotemporal prediction. In Proceedings of the AAAI Conference on Artificial Intelligence, New York, NY, USA, 7–12 February 2020; pp. 11531–11538.
35. Goodfellow, I.; Pouget-Abadie, J.; Mirza, M.; Xu, B.; Warde-Farley, D.; Ozair, S.; Courville, A.; Bengio, Y. Generative adversarial networks. *Commun. ACM* **2020**, *63*, 139–144. [CrossRef]
36. Liu, Z.; Lin, Y.; Cao, Y.; Hu, H.; Wei, Y.; Zhang, Z.; Lin, S.; Guo, B. Swin transformer: Hierarchical vision transformer using shifted windows. In Proceedings of the IEEE/CVF International Conference on Computer Vision, Montreal, BC, Canada, 11–17 October 2021; pp. 10012–10022.
37. Wang, J.Z.; Chen, J.; Xue, H.L.; Li, H.Q.; Zhang, H.B. The roles of small-scale topographic perturbations in precipitation forecasting using a convectio05-004n-permitting ensemble prediction system over southern China. *Q. J. R. Meteorol. Soc.* **2022**, *148*, 2468–2489. [CrossRef]
38. Pan, J.; Teng, D.; Zhang, F.; Zhou, L.; Luo, L.; Weng, Y.; Zhang, Y. Dynamics of local extreme rainfall of super Typhoon Soudelor (2015) in East China. *Sci. China Earth Sci.* **2018**, *61*, 572–594. [CrossRef]

39. Chen, L.; Wang, K.; Li, J.; Li, D. Causality analysis of precipitation anomaliesover Zhejiang province in November 2015. *J. Meteorol. Sci.* **2017**, *37*, 542–552.
40. Lou, X.; Ma, H.; Huang, X.; Liu, H.; Peng, X. Analysis on the causes of extreme precipitation by typhoon "Lekima"(1909) in Zhejiang Province. *J. Meteorol. Sci.* **2020**, *40*, 78–88.